Title

Coupled Axisymmetric Thermo-Poro-Mechanical Finite Element Analysis of Energy Foundation Centrifuge Experiments in Partially Saturated Silt

Journal

Geotechnical and Geological Engineering, 33(2)

ISSN

0960-3182

Authors

Wang, W
Regueiro, RA
McCartney, JS

Publication Date

2015-04-01

DOI

10.1007/s10706-014-9801-4

Peer reviewed

Coupled axisymmetric thermo-poro-mechanical finite element analysis of energy foundation centrifuge experiments in partially saturated silt

W. Wang*, R.A. Regueiro and J. S. McCartney
Department of Civil, Environmental, and Architectural Engineering
University of Colorado, Boulder
Boulder, CO 80309

December 2, 2013

Abstract

The paper presents an axisymmetric, small strain, fully-coupled, thermo-poro-mechanical (TPM) finite element analysis (FEA) of soil-structure interaction (SSI) between energy foundations and partially saturated silt. To account for the coupled processes involving the mechanical response, gas flow, water species flow, and heat flow, nonlinear governing equations are obtained from the fundamental laws of continuum mechanics, based on mixture theory of porous media at small strain. Constitutive relations consist of the effective stress concept, Fourier's law for heat conduction, Darcy's law and Fick's law for pore liquid and gas flow, and both nonlinear elastic and elasto-plastic constitutive models for the soil solid skeleton based on a critical state soil mechanics framework. The constitutive parameters employed in the thermo-poro-mechanical FEA are mostly fitted with experimental data. To validate the TPM model, the numerical results are compared with the observations of centrifuge-scale tests on semi-floating energy foundations in compacted silt. Variables measured include the thermal axial strains and temperature in the foundations, surface settlements, and volumetric water contents in the surrounding soil. Good agreement is obtained between the experimental and model results. Thermally-induced liquid water and water vapor flow inside the soil were found to have an impact on soil-structure interaction. With further improvements (including interface elements at the foundation-soil interface), FEA with the validated thermo-poro-mechanical model can be used to predict performance and soil-structure interaction mechanisms for energy foundations.

keywords: partially saturated soils; thermo-poro-mechanics; FEM; axisymmetric; multiphase flow; energy foundation.

*wei.wang-2@colorado.edu, corresponding author

1 Introduction

Energy foundations are becoming more popular as an energy-saving and environmentally-friendly technology. With adequate design and installation, energy foundations can fulfill not only the geotechnical but also the thermal requirements of buildings without relying solely on conventional heating and cooling systems; hence, energy consumption can be reduced, as well as carbon dioxide emissions [Brandl, 1998, Ennigkeit and Katzenbach, 2002, Lund et al., 2004]. Most energy foundations involve heat exchangers attached to the inside of the reinforcement cage of drilled shafts [Brandl, 2006]. By fully utilizing the steady ground temperature and the thermal properties of concrete, buildings can be heated and cooled through energy foundations with heat pumps at very low cost [Hughes, 2008, Preene and Powrie, 2009].

Research were conducted by means of full-scale field tests and centrifuge-scale tests to investigate the mechanisms of thermo-mechanical soil-structure interaction. The distribution of thermally induced axial strain and stress were evaluated in energy foundations by different approaches [Laloui et al., 2006, Bourne-Webb et al., 2009, McCartney and Rosenberg, 2011, Amatya et al., 2012, McCartney and Murphy, 2012]. In addition, investigations showed that heat and water (liquid/vapor) flow induced by the operation of energy foundation systems occurs in the surrounding soil. Rees et al. [2000] explained that conduction, convection, and latent heat of vaporization are the main mechanisms of heat transfer in porous media; radiation is usually negligible. The efficiency of this heat transfer greatly depends on soil type, temperature, and suction gradients [Hepbasli, 2003].

A number of theoretical models were proposed to account for the heat and moisture transfer in partially saturated soil, assuming the solid skeleton is rigid [Philip and de Vries, 1957, de Vries, 1958, Milly, 1982, Bear et al., 1991, Thomas and Sansom, 1995]. Extended models were developed to take into account the elastic deformation of the soil solid skeleton [Thomas and He, 1995, Gawin et al., 1995, Thomas and He, 1997, Thomas and Missoum, 1999]. Further, Khalili and Loret [2001], Laloui and Cekerevac [2003], François and Laloui [2008] proposed modified Cam-Clay models to include temperature as an additional state variable of the yield function. Many

attempts were made to experimentally explore thermal effects on the hydro-mechanical behavior of partially saturated soils. Romero et al. [2001] studied temperature effects on the water retention curve and permeability of partially saturated clays. Wu et al. [2004], Uchaipichat and Khalili [2009] designed experiments to investigate the thermal softening phenomenon of a partially saturated clay, and discovered decreases in the pre-consolidation pressure during the heating process.

Although some observations have been obtained from field studies, issues that are still not well understood are the complex interactions among temperature change, induced effective stress, and pore fluid flow in partially saturated soils. For example, thermal expansion and contraction of foundations, thermally-induced volume change of soil, and thermally-induced water flow may lead to the changes in the effective stress state and soil-foundation side shear resistance, thus affecting the mechanical response of energy foundations and their long-term structural performance.

The paper employs an axisymmetric small strain, fully-coupled TPM finite element (FE) model to simulate soil-structure interaction (SSI) between energy foundations and partially saturated silt. We present briefly the formulation of the fully-coupled thermo-poro-elasto-plastic FE model. The governing equations are developed based on the mixture theory of porous media, and satisfy the balance of mass, linear momentum and energy conservation, as well as reduced dissipation inequality derived from the second law of thermodynamics. Solid and liquid water are assumed to be isotropic and mechanically-incompressible, yet the soil solid skeleton is compressible; individual constituents can thermally expand or contract. The model is implemented for small strain analysis. Darcy's law is employed to express the advection of water and bulk gas flow through porous media, and the diffusion of vapor and dry air through the gas is governed by Fick's law. Fourier's law is assumed for heat conduction through the soil mixture. The model of van Genuchten [van Genuchten, 1980] was used to represent the soil-water retention curve (SWRC). Nodes of the energy foundation and soil meshes at the interface are assumed to have no relative displacement in this implementation (rigid connection), although this assumption will be relaxed in future work by considering a TPM interface element. Interpolations for a 9-noded isoparametric mixed quadrilateral element are biquadratic for displacement and bilinear for pore water, pore gas pressure and

temperature to model the coupling effects (see Figure 1).

Notation: Bold-face letters denote matrices, tensors and vectors. The symbol "$\cdot$" denotes an inner product of two vectors ($\boldsymbol{a} \cdot \boldsymbol{b} = a_i b_i$), or a single contraction of adjacent indices of two tensors ($(\boldsymbol{c} \cdot \boldsymbol{d})_{ik} = c_{ij} d_{jk}$). The double contraction symbol ":" works similarly, such that $\boldsymbol{c} : \boldsymbol{d} = c_{ij} d_{ij}$ or $(\boldsymbol{A} : \boldsymbol{x})_{ij} = A_{ijkl} x_{kl}$. Summation is implied on repeated indices. Superscript "α" refers to constituent α, which can be solid (s), liquid water (w), dry air (ga) or water vapor (gv) for partially saturated porous media. Material time derivative with respect to the motion of constituent α is written as $\frac{D^\alpha(\bullet)}{Dt} = \frac{\partial(\bullet)}{\partial t} + \text{grad}(\bullet) \cdot \boldsymbol{v}_\alpha$, where $\boldsymbol{v}_\alpha$ is the absolute velocity of constituent α, and $(\bullet)$ indicates any variable. Cylindrical coordinates are employed, with the vector of coordinates $\boldsymbol{r} = [r, z]$. Solid mechanics sign convention is used, i.e. positive stress σ and positive strain ε for tension. The pore water pressure is positive in compression.

2 Governing Equations and Constitutive Models

Based on the mixture theory of porous media, the paper briefly describes a coupled thermo-poro-elasto-plastic model for partially saturated soil under a number of assumptions that are summarized in detail by Wang [2014]. First, the partially saturated soil is treated as a three-phase mixture, i.e. solid phase, liquid phase and gas phase. The liquid phase here specifically refers to liquid water, as we ignore the dissolved air. The gas phase is treated as an ideal gas mixture composed of water vapor and dry air. The solid and liquid phases are isotropic and mechanically incompressible, but can expand under temperature increase or contract under temperature decrease. The soil solid skeleton is deformable mechanically, and an elasto-plastic constitutive model is adopted to model its deformable behavior. The pore space of the solid skeleton is filled partially with liquid and gas. Local thermal equilibrium is assumed to be achieved instantaneously among all the phases, which requires that the movement of fluid (water or gas) is sufficiently slow, and the surface areas of all phases are sufficiently large [Neaupane and Yamabe, 2001, Abdel-Hadi and Mitchell, 1981]. In other words, the temperature of each phase equals each other, i.e., $\theta^s = \theta^w = \theta^g = \theta$, therefore, only

the temperature of the soil mixture θ needs to be solved.

According to the principles of continuum mechanics, governing equations are derived based on the balance laws for mass, momentum, energy, as well as the second law of thermodynamics, which applies the restriction on the form of the constitutive equations.

As for the choice of primary variables, there are several possible combinations [Lewis and Schrefler, 1998], one of which is used in this paper: solid skeleton displacement vector $\boldsymbol{u}$, temperature of soil mixture θ, pore water pressure p_w, and pore gas pressure p_g. Other standard concepts from mixture theory [Coussy, 2004, de Boer, 2005] are employed, such as the volume of the mixture is the sum of the volumes of each phase, $v = v_s + v_w + v_g$; the volume fraction of α phase ($\alpha = s(solid), w(water), g(gas)$) is defined as $n^\alpha = dv_\alpha / dv$, and $n_w + n_g + n_s = 1$, the porosity n for partially saturated porous media is defined as the sum of the water and gas volume fractions, i.e., $n = n_w + n_g$; the partial mass density of α phase is defined as $\rho^\alpha = n^\alpha \rho^{\alpha R}$, where $\rho^{\alpha R}$ is true mass density of α phase, e.g. for liquid water phase, $\rho^{wR} = 998 kg/m^3$ at $\theta \approx 20^o C$, therefore, the total density of the porous medium can be written in terms of the partial mass densities of the individual phases as $\rho = \rho^s + \rho^w + \rho^g$.

2.1 Balance of mass equation for water species (liquid water + water vapor)

The balance of mass equations are derived with respect to each constituent $\alpha = s, w, gv, ga$ independently. The details are omitted here, but we arrive at the usual localized form of the balance of mass for constituent α as

$$\frac{D^\alpha \rho^\alpha}{Dt} + \rho^\alpha \, \mathrm{div} \boldsymbol{v}^\alpha = \hat{\rho}^\alpha \tag{1}$$

where "div" is the divergence operator, and $\hat{\rho}^\alpha$ is the mass exchange on α from other constituents. Summing the equations of liquid water and water vapor yields the balance of mass equation for the water species. Using the balance equation of the solid to eliminate the material time derivative of

porosity gives the complete form as follows:

$$(\rho^{wR}S_w+\rho^{gvR}S_g)\mathrm{div}\,\boldsymbol{v}_s+n(\rho^{wR}-\rho^{gvR})\frac{D^sS_w}{Dt}+nS_g\frac{D^s\rho^{gvR}}{Dt}$$
$$-\left[(1-n)(\rho^{wR}S_w+\rho^{gvR}S_g)\beta_s^\theta+n\rho^{wR}S_w\beta_w^\theta\right]\frac{D^s\theta}{Dt}+\mathrm{div}(\rho^{gvR}\tilde{\boldsymbol{v}}_{gv}^s+\rho^{wR}\tilde{\boldsymbol{v}}_w^s)=0 \quad (2)$$

where, ρ^{wR} and ρ^{gvR} are respectively true mass densities of liquid water and water vapor; β_w^θ and β_s^θ are respectively thermal expansion coefficients of liquid water and solid; S_w and S_g are respectively the degrees of saturation for water and gas, and $S_w=n_w/n$, $S_g=1-S_w$. The material time derivative with respect to solid (s) phase is given by

$$\frac{D^s(\bullet)}{Dt}=\frac{\partial\bullet}{\partial t}+\mathrm{grad}(\bullet)\cdot\boldsymbol{v}_s \quad (3)$$

where $\boldsymbol{v}_s$ = solid skeleton velocity, which is defined as the material time derivative of the displacement $\boldsymbol{u}$ of the solid skeleton: $\boldsymbol{v}_s=\frac{D^s\boldsymbol{u}}{Dt}$.

S_w is assumed to be related to matric suction $s=p_g-p_w$ through the van Genuchten model [van Genuchten, 1980], :

$$S_e=\frac{S_w-S_r}{1-S_r}=\left[\frac{1}{1+(s/a)^m}\right]^{(1-1/m)} \quad (4)$$

where S_e = the effective degree of saturation; S_r = the residual degree of saturation; a and m are fitting parameters, then

$$\frac{D^sS_w}{Dt}=\frac{\partial S_w}{\partial s}\frac{D^ss}{Dt}=\frac{\partial S_w}{\partial s}\left(\frac{D^sp_g}{Dt}-\frac{D^sp_w}{Dt}\right) \quad (5)$$

Darcy's velocity of liquid water $\tilde{\boldsymbol{v}}_w^s$ =$n_w(\boldsymbol{v}_w-\boldsymbol{v}_s)$ is given by Darcy's law [Coussy, 2004]:

$$\tilde{\boldsymbol{v}}_w^s=-\frac{\kappa(n)K_{rw}(S_w)}{\mu_w(\theta)}(\nabla p_w-\rho^{wR}\boldsymbol{g}) \quad (6)$$

where, $K_{rw}(S_w)$ = relative permeability of the water phase as given by [van Genuchten, 1980]:

$$K_{rw}(S_e) = \sqrt{S_e}\left[1-(1-S_e^{\frac{1}{m}})^m\right]^2 \tag{7}$$

$\mu_w(\theta)$ = dynamic viscosity of water at temperature θ. $\kappa = l^2\delta(n)$ = the intrinsic permeability of the skeleton, which depends only on the porous network geometry, where l is assumed to characterize the porous network geometry as far as the porous media is saturated with one fluid for simple geometries. A common expression of $\delta(n)$ is the Kozeny-Carman formula given as: $\delta(n) = n^3/(1-n^2)$.

As a component of the gas mixture, water vapor is transported by both advection governed by Darcy's law and molecular diffusion governed by Fick's law. Therefore, the apparent velocity of water vapor $\tilde{v}_{gv}^s$ is [Coussy, 2004]:

$$\widetilde{v}_{gv}^{s} = -\frac{\kappa(n)K_{rg}}{\mu_g(\theta)}\nabla p_g - D\,\nabla[\ln\left(\frac{p_{gv}}{p_g}\right)] \tag{8}$$

where, $K_{rg}(S_w)$ = relative permeability of gas phase given as

$$K_{rg}(S_e) = \sqrt{1-S_e}\left(1-S_e^{\frac{1}{m}}\right)^{2m} \tag{9}$$

$\mu_g(\theta)$ = dynamic viscosity of gas at temperature θ; p_{gv} = vapor pressure, as given by the ideal gas law:

$$p_{gv} = \frac{\rho^{gvR}\theta R}{M_w} \tag{10}$$

D= diffusion coefficient expressed as

$$D = (n_g\,\tau)D_0\,\frac{p_{atm}}{p_g};\quad D_0 = \delta_0\left(\frac{\theta}{\theta_0}\right)^{1.88} \tag{11}$$

where, the parameters involved are obtained through experiments [de Vries and Kruger, 1966]: $\delta_0 = 2.17\times10^{-5}m^2s$ at $\theta_0 = 273K$, and $p_{atm} = 101325Pa$. The parameter τ is the tortuosity.

Note $\rho^{gvR}\tilde{\boldsymbol{v}}^s_{gv}$ and $\rho^{wR}\tilde{\boldsymbol{v}}^s_w$ in (2) are the mass fluxes of water vapor and liquid water respectively. $\rho^{gvR}\tilde{\boldsymbol{v}}^s_{gv}+\rho^{wR}\tilde{\boldsymbol{v}}^s_w=0$ is required for an equilibrium of fluid flow to be achieved.

2.2 Balance of mass equation for dry air

Different from water vapor, mass is conserved within the dry air. For the sake of brevity, the balance of mass equation may be derived as

$$\begin{aligned}&\rho^{gaR}S_g\mathrm{div}\,\boldsymbol{v}_s-\rho^{gaR}S_g\beta_s^{\theta}(1-n)\frac{D^s\theta}{Dt}+nS_g\frac{D^s\rho^{gaR}}{Dt}\\&-n\rho^{gaR}\frac{D^sS_w}{Dt}+\mathrm{div}(\rho^{gaR}\tilde{\boldsymbol{v}}^s_{ga})=0\end{aligned}\tag{12}$$

where, ρ^{gaR} = real density of dry air. As the other component of gas mixture, the apparent velocity of dry air follows the similar format of (8):

$$\tilde{\boldsymbol{v}}^s_{ga}=-\frac{\kappa(n)K_{rg}}{\mu_g(\theta)}\nabla p_g+D\,\nabla[\ln\left(\frac{p_{ga}}{p_g}\right)]\tag{13}$$

where, p_{ga} = dry air pressure. According to Dalton's law of additivity of partial pressures and densities, the pressure and density of gas can be written as

$$\rho^g=\rho^{gv}+\rho^{ga},\quad p_g=p_{gv}+p_{ga}\tag{14}$$

2.3 Balance of linear momentum equation for soil mixture

Considering water vapor and dry air together as the gas (g) phase and ignoring inertia terms[de Boer, 2005], the local form of the balance of linear momentum equation for each phase $\alpha(\alpha=s,w,g)$ is given as

$$\nabla\cdot\boldsymbol{\sigma}^{\alpha}+\rho^{\alpha}\boldsymbol{b}^{\alpha}+\hat{\boldsymbol{h}}^{\alpha}=\hat{\rho}^{\alpha}\boldsymbol{v}_{\alpha}\tag{15}$$

where, $\boldsymbol{\sigma}^{\alpha}$ is the partial stress of the α phase, $\boldsymbol{\sigma}^{\alpha}=n^{\alpha}\boldsymbol{\sigma}$; and the total stress is: $\boldsymbol{\sigma}=\boldsymbol{\sigma}^s+\boldsymbol{\sigma}^w+\boldsymbol{\sigma}^g$; $\boldsymbol{b}^{\alpha}$ is the body force vector per unit mass of α phase, which we assume is equal to acceleration of

gravity: $\boldsymbol{b}^{\alpha} = \boldsymbol{b} = \boldsymbol{g}$; $\hat{\boldsymbol{h}}^{\alpha}$ is internal body force drag by other phases on phase α, and

$$\sum_{\alpha=s,w,g} \hat{\boldsymbol{h}^{\alpha}} = \boldsymbol{0} \tag{16}$$

Mass exchange inertia term $\sum(\hat{\rho}^{\alpha}\boldsymbol{v}_{\alpha})$ is usually ignored [de Boer, 2005]. Adding the equations for the three phases yields the complete balance of linear momentum equation for the soil mixture:

$$\mathrm{div}(\boldsymbol{\sigma}) + \rho\boldsymbol{g} = \boldsymbol{0} \tag{17}$$

To relate the total stress tensor $\boldsymbol{\sigma}$ and the effective stress tensor of the solid skeleton $\boldsymbol{\sigma}'$ for partially saturated soil, Bishop's effective stress factor χ is adopted [Bishop, 1959]. Therefore,

$$\boldsymbol{\sigma}' = (\boldsymbol{\sigma} + p_g\,\boldsymbol{1}) - \chi(p_g - p_w)\,\boldsymbol{1} \tag{18}$$

where, the sign convention follows the the rule of solid mechanics, i.e. positive for tension. The expression $\chi = S_w$ proposed by Bishop and Blight [1963], Lewis and Schrefler [1998], Borja [2004] is employed here. Equation (18) will reduce to the classic saturated effective stress equation by setting $\chi = 0$ for perfectly dry soils, or $\chi = 1$ for saturated soils. The evolution for $\boldsymbol{\sigma}'$ is through a nonlinear elasto-plastic Cam-Clay model for partially saturated soil [Borja, 2004] extended for temperature-dependent pre-consolidation stress p_c [Laloui and Cekerevac, 2003, Wang, 2014].

2.4 Energy conservation equation for soil mixture

To obtain the energy conservation equation for the soil mixture, the local form of the energy conservation equation for each phase is derived. For the α phase [de Boer, 2005]:

$$\rho^{\alpha}\frac{D^{\alpha}e^{\alpha}}{Dt} - \boldsymbol{\sigma}^{\alpha} : \frac{D^{\alpha}\boldsymbol{\epsilon}^{\alpha}}{Dt} + \hat{\boldsymbol{h}}^{\alpha}\cdot\boldsymbol{v}_{\alpha} - \rho^{\alpha}r^{\alpha} + \mathrm{div}\boldsymbol{q}^{\alpha} + \hat{\rho}^{\alpha}e^{\alpha} - \hat{e}^{\alpha} = 0 \tag{19}$$

where, for phase α, e^{α} = internal energy per unit mass; r^{α} = internal heat source per unit mass; $\hat{e}^{\alpha}$ = energy supply rate to α phase caused by all other constituents; $\boldsymbol{q}^{\alpha}$ = heat flux vector, generally,

it includes three terms, i.e., heat conduction, convection and heat radiation. For now we only consider heat conduction, for which the Fourier's law is assumed to be valid: $\boldsymbol{q}^{\alpha} = -\boldsymbol{K}_{\alpha}^{\theta} \operatorname{grad} \theta$, where $\boldsymbol{K}_{\alpha}^{\theta}$ = the thermal conductivity matrix of the α phase.

Adding the energy conservation equations of all phases yields the energy conservation equation for the soil mixture, with details omitted, as

$$(\rho C)_m \frac{D^s \theta}{Dt} + \rho^{wR} C^w \tilde{\boldsymbol{v}}_w^s \cdot \operatorname{grad} \theta + \rho^{gR} C^g \tilde{\boldsymbol{v}}_g^s \cdot \operatorname{grad} \theta - \rho r + \operatorname{div} \boldsymbol{q} + \hat{\rho}^{gv} H_{vap} = 0 \qquad (20)$$

where, $(\rho C)_m = \rho^s C^s + \rho^w C^w + \rho^g C^g$, and C^s, C^w, and C^g are respectively the specific heat capacity of the solid, water and gas phases; ρr = total heat source in soil mixture; $\boldsymbol{q}$ = total heat flux vector; and the mass exchange term $\hat{\rho}^{gv}$ due to phase change can be obtained from the balance of mass equation of either liquid water or water vapor.

Equations (2), (12), (17), and (20) are solved in a fully-coupled manner using the nonlinear FE method at small strain.

3 Coupled Finite Element Formulation

The model involves three main physical processes: non-isothermal pore liquid (water) and gas flow, soil mixture heat transport, and poroelasto-plastic deformation. The corresponding field variables are soil solid-skeleton displacement $\boldsymbol{u}$, pore water pressure p_w, pore gas pressure p_g, and soil mixture temperature θ solved at the nodes of the FE mesh (in Figure 5).

The method of weighted residuals is applied to formulate the coupled variational equations from the coupled governing differential equations, which are then discretized using finite elements in an axisymmetric formulation. Quadrilateral finite elements with biquadratic interpolation in solid-skeleton displacement, bilinear in pore water pressure, pore gas pressure, and soil mixture temperature are employed to ensure numerical stability. Weighting functions $w_i(\boldsymbol{r})$, $\eta(\boldsymbol{r})$, $\omega(\boldsymbol{r})$ and $\varphi(\boldsymbol{r})$ are used for displacement, pore water pressure, pore gas pressure, and soil mixture temperature, respectively. We employ isoparametric interpolations [Hughes, 1987] with shape func-

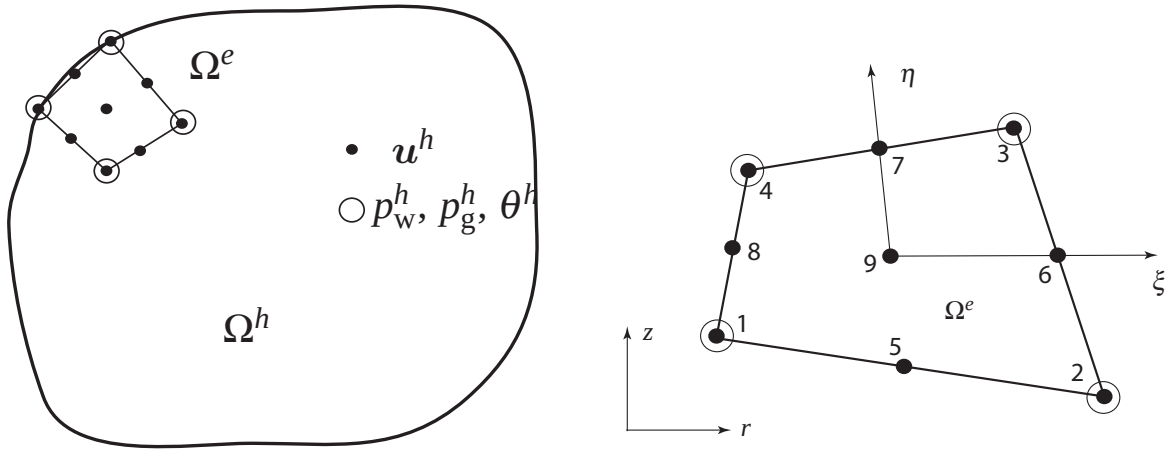

Figure 1. Discretization into mixed quadrilateral elements.

tions $\boldsymbol{N}^u$ for displacement, and $\boldsymbol{N}^p$ for pore water and gas pressure and soil mixture temperature, such that

$$\boldsymbol{u}^h = \boldsymbol{N}^u \cdot \boldsymbol{d}^e \,, \quad \boldsymbol{w}^h = \boldsymbol{N}^u \cdot \boldsymbol{\phi}^e \tag{21}$$

$$p_w^h = \boldsymbol{N}^p \cdot \boldsymbol{p}_w^e \,, \quad \eta^h = \boldsymbol{N}^p \cdot \boldsymbol{\alpha}^e \tag{22}$$

$$p_g^h = \boldsymbol{N}^p \cdot \boldsymbol{p}_g^e \,, \quad \omega^h = \boldsymbol{N}^p \cdot \boldsymbol{\beta}^e \tag{23}$$

$$\theta^h = \boldsymbol{N}^p \cdot \boldsymbol{\theta}^e \,, \quad \varphi^h = \boldsymbol{N}^p \cdot \boldsymbol{\gamma}^e \tag{24}$$

where *h* implies discretization, and the shape functions matrices are

$$\boldsymbol{N}^u = [\boldsymbol{N}_1^u \cdots \boldsymbol{N}_9^u] \,,\ \boldsymbol{N}_1^u = \begin{bmatrix} N_1^u & 0 \\ 0 & N_1^u \end{bmatrix} \,,\ \boldsymbol{N}^p = [N_1^p \cdots N_4^p] \tag{25}$$

and $\boldsymbol{d}^e$, $\boldsymbol{p}_w^e$, $\boldsymbol{p}_g^e$ and $\boldsymbol{\theta}^e$ are nodal degree of freedom vectors of element solid-skeleton displacement, pore water pressure, pore gas pressure, and soil mixture temperature, with corresponding weight function vectors $\boldsymbol{\phi}^e$, $\boldsymbol{\alpha}^e$, $\boldsymbol{\beta}^e$ and $\boldsymbol{\gamma}^e$. Details aside, we arrive at the coupled nonlinear first order ordinary differential equation to solve, using generalized trapezoidal rule for time integration, and

Newton-Raphson nonlinear solution algorithm.

$$\begin{bmatrix} \mathbf{0} & \mathbf{0} & \mathbf{0} & \mathbf{0} \\ \boldsymbol{K}^{wd} & -\boldsymbol{K}^{wg} & \boldsymbol{K}^{wg} & \boldsymbol{K}^{w\theta} \\ \boldsymbol{K}^{gd} & \boldsymbol{K}^{gw} & \boldsymbol{K}^{gg} & \boldsymbol{K}^{g\theta} \\ \boldsymbol{K}^{\theta d} & \boldsymbol{K}^{\theta g} & -\boldsymbol{K}^{\theta g} & \boldsymbol{K}^{\theta\theta} \end{bmatrix} \begin{Bmatrix} \dot{\boldsymbol{d}} \\ \dot{\boldsymbol{p}}_w \\ \dot{\boldsymbol{p}}_g \\ \dot{\boldsymbol{\theta}} \end{Bmatrix} + \begin{Bmatrix} \boldsymbol{F}^{d,INT} \\ \boldsymbol{F}^{w,INT} \\ \boldsymbol{F}^{g,INT} \\ \boldsymbol{F}^{\theta,INT} \end{Bmatrix} = \begin{Bmatrix} \boldsymbol{F}^{d,EXT} \\ \boldsymbol{F}^{w,EXT} \\ \boldsymbol{F}^{g,EXT} \\ \boldsymbol{F}^{\theta,EXT} \end{Bmatrix} \tag{26}$$

where the $\boldsymbol{K}$'s and $\boldsymbol{F}^{INT}$'s are the various nonlinear coupling matrices and "force" vector functions of $\boldsymbol{d}$, $\boldsymbol{p}_w$, $\boldsymbol{p}_g$ and $\boldsymbol{\theta}$ through the coupling terms, with details omitted here (see Wang [2014]).

4 Centrifuge Physical Model

A series of centrifuge-scale tests were performed on semi-floating energy foundations in partially saturated silt by Goode [2013]. A scale-model energy foundation having a diameter of 63.5 mm and a length of 342.9 mm was fabricated to study the impact of mechanical loading and heating on the internal strain distribution in energy foundations. A centrifuge acceleration of 24g was used throughout this study, so the corresponding prototype-scale foundation length is 8.2 m with a diameter of 1.5 m. However, the FEA in this study was performed in model scale to avoid issues related to the scaling of temperature and diffusive heat transfer in the centrifuge as recommended by Stewart and McCartney [2013].

Seven strain gages and thermocouples were embedded within the foundation to characterize the strain response and temperature distribution within the foundation at the depths shown in the schematic in Figure 2. Three loops of Perfluoroalkoxy (PFA) tubing with an inside diameter of 3.175 mm were used to circulate heated fluid through the foundation. The loops were affixed to the inside of the reinforcing cage so that the inlet and outlet tubes were on the opposite sides of the foundation and so that they did not cross the bottom of the cage. The foundation has a larger diameter than that of Stewart and McCartney [2013] to provide more space around embedded instrumentation and to incorporate a larger fraction and size of coarse aggregates into the concrete

mix design. Although drilled shafts are typically cast-in-place, the model foundation was precast in a cardboard mold with a reinforcement cage having an opening size of 12.7 mm to ensure quality construction considering the extensive instrumentation. This approach also allows for characterization of the mechanical and thermal properties of the foundation. The larger fraction of coarse aggregates led to a Young's modulus of reinforced concrete of 30 GPa that was closer to that of drilled shaft foundations in the field than that of Stewart and McCartney [2013]. The measured coefficient of thermal expansion of the scale-model energy foundation was $16\mu\varepsilon/^oC$, which is greater than that of reinforced concrete in full-scale drilled shaft foundations (typically between 10 and $12\mu\varepsilon/^oC$). Details of the instrumentation calibration are provided by Goode and McCartney [2014].

A cross-sectional profile schematic and a top-view plan schematic of the container used in the centrifuge-scale tests is shown in Figure 3. The container is an aluminum cylinder with an inside diameter of 605 mm, wall thickness of 13 mm, and an inside height of 533.4 mm. The foundation is tested in a soil layer having a thickness of 533.4 mm, so its tip will rest on a layer of compacted silt leading to a semi-floating end restraint boundary condition. The schematics in Figure 3 show the positions of the embedded strain gauges and thermocouples within the foundations, linearly-variable differential transformers (LVDTs) used to measure vertical displacements of the foundation and soil, dielectric sensors used to monitor the volumetric water content and temperature of the surrounding soil, and thermocouple profile probes for measuring the temperature of the soil. A 13 mm-thick insulation sheet is wrapped around the container to minimize heat transfer through the sides of the cylinder, which corresponds with an adiabatic boundary condition on the container surface. The bottom of the container is not insulated in order to provide a stiff platform during mechanical loading. Although a slight heat loss will likely occur from both the top and the bottom of the container, these boundary are assumed to be adiabatic in the FEA for simplicity. Heat convection at the boundaries will be included in future work to provide a more accurate simulation. The top of the container is covered using plastic wrap to minimize loss of fluid and to reduce convective heat transfer at the soil surface. Thus, no water flux at the top of the soil is

assumed in the analysis. In the experiment, the temperature of the energy foundation is controlled by circulating fluid with a known temperature through the heat exchanger tubes attached to the inside of the reinforcement cage at r = 24.25mm, but a constant temperature was applied to this radial location in the FEA.

In the centrifuge-scale experiments, the same scale-model foundation was used in different tests. The tests were performed with identical conditions, except that different temperature changes were applied to the foundation in the different tests. The test procedures involve application of a seating load (600N) in load-control conditions (i.e., zero head stiffness), followed by heating of the foundation to reach a desired temperature. After the head displacements, internal axial strains, and temperature of the foundation stabilized under each change in temperature, the foundation was loaded to failure to define the load-settlement curve. After reaching a load of 3265 N in model scale, the foundation was unloaded. A general schematic of the experimental procedures is shown in Figure 4, and a list of the testing phases is shown in Table 1.

Table 1. Experimental and FE simulation procedure shown in Figure 4.

Phase 1	Consolidation under g-level N =1 in simulation, representing compaction of soil
Phase 2	Spin up centrifuge to a g-level of $N = 24$, wait for equilibration
Phase 3	Apply a seating load at the foundation top, wait for equilibrium
Phase 4	Heating the foundations to different temperatures
Phase 5	Load the foundations to failure, and then unload under different temperatures

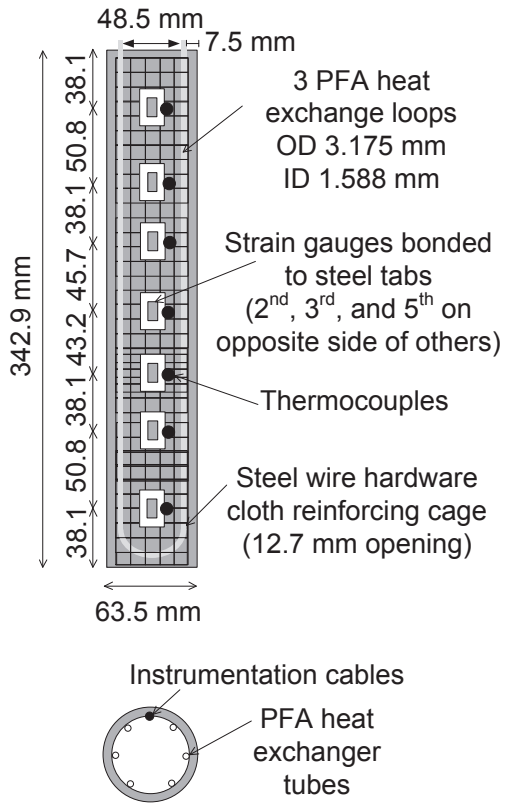

Figure 2. Cross-sections of the scale-model energy foundation [Goode and McCartney, 2014].

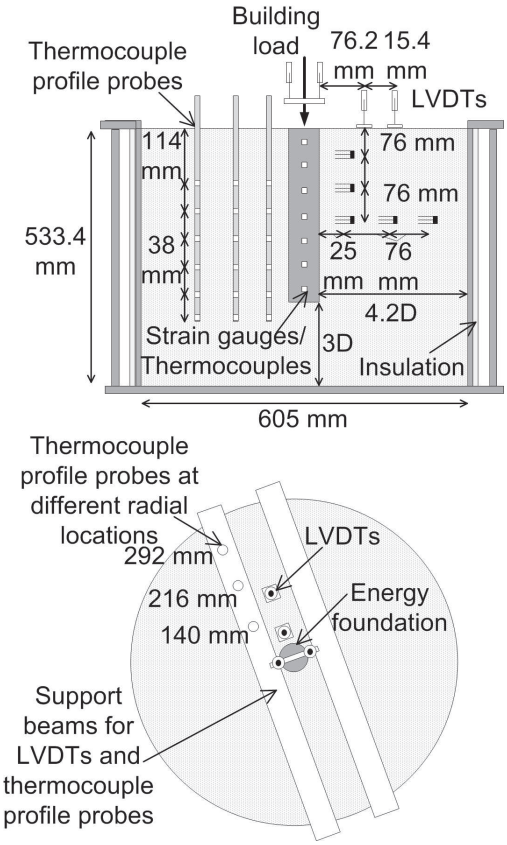

Figure 3. Experimental setup and instrumentation plan [Goode and McCartney, 2014].

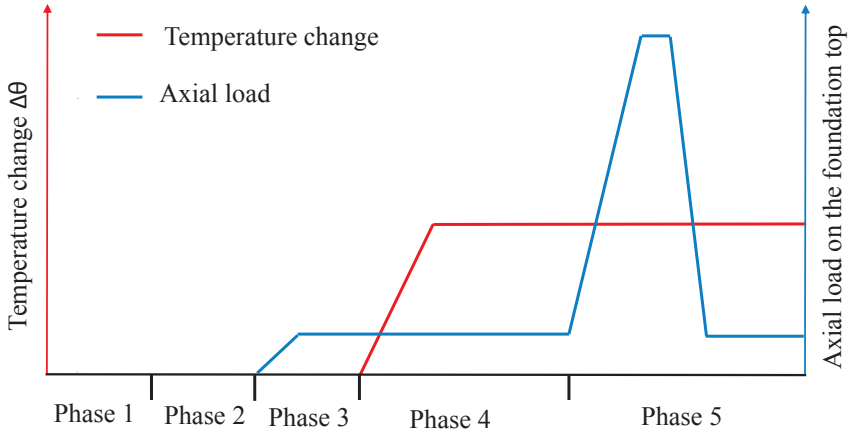

Figure 4. Schematic of general testing procedures for energy foundation centrifuge experiment.

5 Finite Element Model

To simulate SSI of an energy foundation in partially saturated silt under thermal, hydraulic, and mechanical loads in the centrifuge experiments, a simplified axisymmetric FE mesh contains 81 elements, 9 elements in radial *r* direction and 9 elements in axial *z* direction, as shown in Figure 5. The partially saturated soil is modeled as an overconsolidated soil layer with thermo-elasto-plastic behavior. The geometry of the FE model (Figure 5) is the same as the experimental samples. The heights of the semi-floating foundation and the container are 342.9*mm* and 533.4*mm*, respectively.

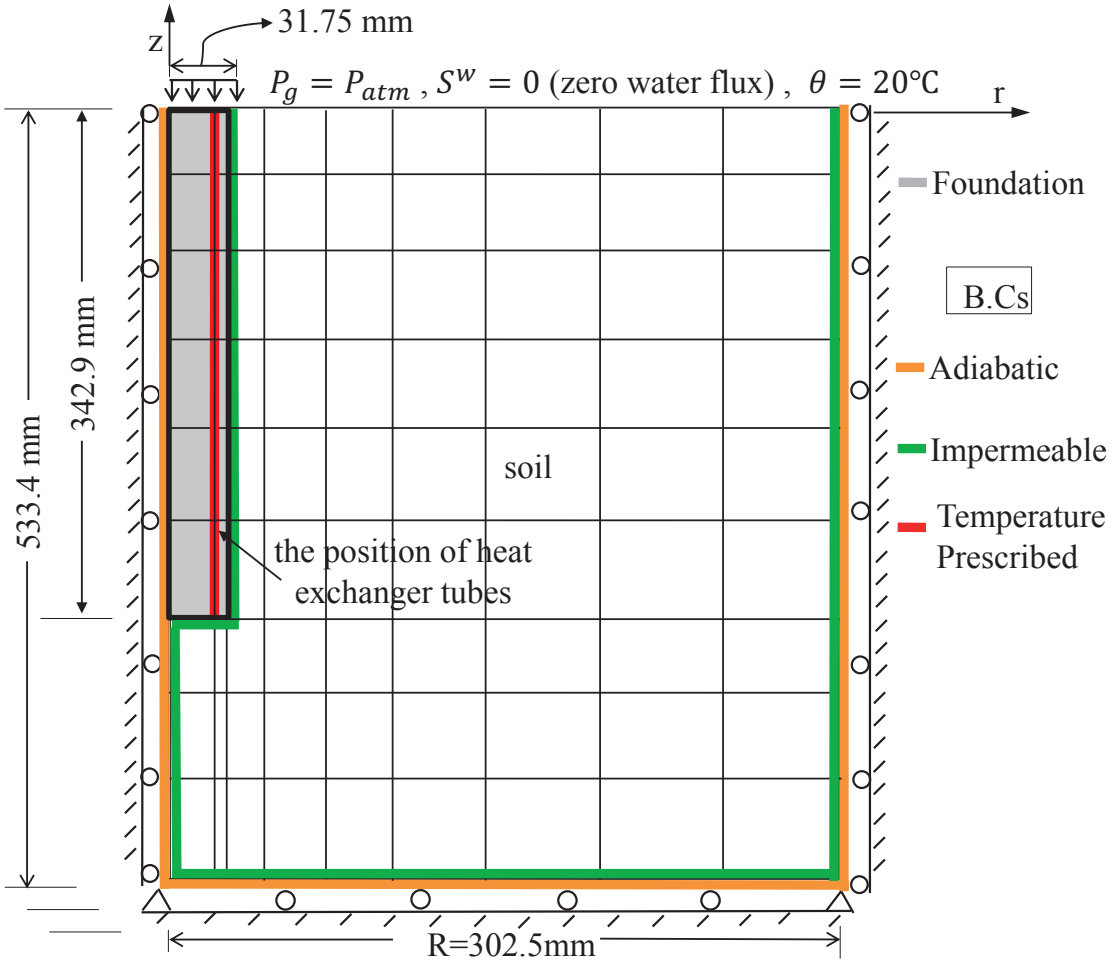

Figure 5. Axisymmetric FE mesh and geometry for simulating end-bearing energy foundation centrifuge experiment. Boundary conditions are included.

Boundary conditions and initial conditions are simplified according to knowledge of the experimental conditions. The initial conditions are shown in Table 3. As for boundary conditions, due to

the axisymmetry of the problem, and assumed rigidity of the bucket, nodal displacements on the z axis ($r = 0$) and right edge ($r = R$) are $u_r = 0$, and nodal displacements on the bottom ($z = -H$) are $u_z = 0$. An unreinforced concrete energy foundation is assumed to be impermeable in this analysis. For now, on the top of the soil, we assume zero water flux $S^w = 0$, and the pore gas pressure being kept to be atmospheric pressure $p_g = p_{atm}$. We notice that the assumption of undrained boundary condition for pore water pressure and drained boundary condition for pore gas pressure at the top may not be justified, but it will be improved in future work when we consider soil-atmosphere interaction to account for evaporation fluxes.To mimic the heating condition of the circulating fluid through the "U" shape heat exchanger tubes, we assume that temperature is prescribed along the z axis at $r = 24.25mm$ for simplicity. However, technically, a 3-D model including a computational fluid dynamics (CFD) analysis of the heated fluid flow through the tubes would be a more accurate estimate of the thermal boundary condition. During circulation of heated fluid through the heat exchange elements in the foundation, energy foundations typically reach a relatively constant temperature with depth. This has been observed in several previous laboratory studies [Stewart and McCartney, 2013]. The constant temperature conditions were selected in the study to evaluate the thermo-mechanical soil-structure interaction behavior of the foundation, not to evaluate the transient heat transfer processes, which we believe would be better simulated with a heat flux boundary condition. The temperature at the top of the soil is held constant at room temperature (20 °C, 293 K), and the other surfaces are adiabatic as indicated in Figure 5. Corresponding to the seating load ($600N$), a corresponding effective solid-skeleton traction $\boldsymbol{t}^{\sigma'} = [0 \ -t^{\sigma'}]$, $t^{\sigma'} = 189kPa$, is applied on the top of the energy foundation. During Phase 5, a load of $3645N$ was applied to simulate the load to fail the foundation [Goode, 2013]. The parameters of the reinforced concrete energy foundation (F) and soil (Table 2) are determined from experimental measurements [Goode, 2013]. Fluid parameters are assumed for water. In addition, the paper refers to Borja [2004] for certain elasto-plastic parameters of the soil that are not tested in the experiment.

The simulation of the centrifuge experiments is part of the validation process of the TPM model. After the model is further improved and validated, FEA can be combined with the cen-

trifuge experiments to obtain a comprehensive understanding of the fundamental soil mechanics phenomena involved in energy foundations. With this knowledge, we may assess the potential issues, evaluate the long-term performance and sustainability, thereby providing practical design guidance for energy foundations.

Table 2. Parameters used in the FEA.

Parameter	Symbol	Value	Unit
Linear thermal expansion coefficient of energy foundation	β_F^θ	16×10^{-6}	$/K$
Linear thermal expansion coefficient of solid skeleton	β_{skel}^θ	8.7×10^{-6}	$/K$
Linear thermal expansion coefficient of solid	β_s^θ	1.17×10^{-5}	$/K$
Linear thermal expansion coefficient of water	β_w^θ	6.9×10^{-5}	$/K$
Specific heat capacity of energy foundation	C_F	855	$J/(K \cdot kg)$
Specific heat capacity of solid	C_s	1000	$J/(K \cdot kg)$
Specific heat capacity of water	C_w	4180	$J/(K \cdot kg)$
Mass density of energy foundation	ρ_F	2564	kg/m^3
Specific gravity of soil solids	G_s	2.6	
Thermal conductivity of reinforced concrete	K_F^θ	1.978	$W/(m \cdot K)$
Thermal conductivity of soil mixture	K_s^θ	1.24	$W/(m \cdot K)$
Young's modulus of reinforced concrete	E_F	30×10^9	Pa
Poisson's ratio of energy foundation	ν_F	0.18	m/m
van Genutchen model parameter	a	19.4×10^3	Pa
van Genutchen model parameter	m	1.8	
Intrinsic permeability of soil mixture	κ	1.22×10^{-14}	m^2
Initial mean effective preconsolidation pressure	p_c'	100×10^3	Pa
Initial mean effective pressure	p_0'	70×10^3	Pa
Elastoplastic parameter (slope of critical state line)	M	1.305	
Elastoplastic parameter (slope of isotropic normal compression line)	$\tilde{\lambda}$	0.14	
Elastoplastic parameter (slope of isotropic recompression line)	$\tilde{\kappa}$	0.034	
Thermoplastic parameter	γ^θ	0.04	

Table 3. Initial conditions for soil used in FEA.

Porosity	0.4
Volumetric water content	0.226
Suction	$30\,kPa$
Gas pressure	$101\,kPa$
Temperature	$20^oC(293K)$

6 Results

Contour plots show various results on the deformed mesh with displacement magnification factor equal to 100. Temperature contours (Figures 6, 8, and 10) indicate that although the foundation reaches steady-state temperature at the end of each test, the soil is not necessarily at steady-state temperature, for example, soil mixture temperature remains near the initial value $\theta_0 = 20^oC(293K)$ at further radial distance in the soil. This means that the system response is representative of transient heating, meaning the soil mixture temperature is still evolving. The modeling results of thermal axial strains $\varepsilon_{zz}^{\theta}$ within the foundation are compared with experimental data collected by the strain gauges in Figure 18. Good agreement is observed in the comparison throughout the energy foundation. Note that, different from the sign conventions used by Stewart and McCartney [2013] and Goode [2013], positive strains are used to denote elongation of a foundation or soil element (e.g., due to application of tension or due to thermal expansion), the coefficient of thermal expansion is defined as a positive value, and a positive settlement is defined as an upward heave. Here, the so-called "thermal axial strain" should not be confused with the term we usually use, which is defined as $\varepsilon^{\theta} = \beta^{\theta}\Delta\theta$. In this paper particularly, the thermal axial strain $\varepsilon_{zz}^{\theta}$ actually is the total vertical strain at the end of temperature increase ε_{zz} zeroed out by subtracting the total vertical strain caused by mechanical effects ε_{zz}^{mech} including the gravity and building load, i.e., $\varepsilon_{zz}^{\theta} = \varepsilon_{zz} - \varepsilon_{zz}^{mech}$. The energy foundation achieves almost uniform thermal axial strain distribution except at the bottom where much smaller thermal strain is observed. It is understandable because the thermal expansion of the foundation bottom is partially constrained by the soil resistance underneath. Also, as shown in the temperature contours, the temperature at the foundation bottom is always relatively lower than the upper region due to the contact with the underneath soil. While, for the foundation top, we can conclude that it almost expands freely under thermal loading, based on the fact that the strain values are approximately equal to the calculation by free thermal expansion $\varepsilon^{\theta} = \beta^{\theta}\Delta\theta$. Figures 7, 9 and 11 show that thermal axial strains inside the soil vary more noticeably. Temperature increases cause expansion of the soil near the foundation-soil interface ($31.75mm < r < 132.75mm$). Negligible positive expansive axial strains are observed at further

radial distance. The negative compressive axial strains within the soil underneath the foundation imply that the compression due to the building load on the top of the foundation is dominant, compared to the thermal expansion.

Figures 12 and 13 indicate significant changes in suction and volumetric water content respectively near the soil-foundation interface. For example, volumetric water content decreases from an initial value of 0.226 to approximately 0.18 near the interface ($r = 31.75mm$), and a small rise occurs in the soil at $r = 56.75mm$. Volumetric water contents increase slightly in the region of $56.75mm < r < 92mm$, however, no significant variation is observed beyond $r = 92mm$. Figure 14 indicates that a net rate of evaporation is produced within the soil due to rapidly increasing temperatures. A sharp rise of water vapor pressure (from initial value of $2.5kPa$ to around $6.5kPa$) happens near the soil-foundation interface ($r = 31.75mm$), and a smaller rise occurs further from the interface. The formed density gradients drive vapor from the hotter region (soil-foundation interface) to the cooler region. Arrows in Figure 16 show the direction of water vapor flow inside the soil. Also, higher vapor velocity is observed under larger temperature gradients. This diffusion process is governed by many factors including hydraulic and thermal properties of soil, which require further research. Condensation occurs when the hotter vapor migrates to the region of lower temperature, and hence leads to a rise in volumetric water content, as shown in Figure 13 at $56.75mm < r < 92mm$. As the soil near the soil-foundation interface becomes drier ($p_w \approx 60kPa$ at $r = 31.75mm$) compared to the soil further from the interface (p_w approaches $75kPa$ at $56.75mm$), pore water pressure gradients are formed, which force liquid water to flow from the wetter region to the drier region, as shown in Figure 15. The movement of pore water is illustrated by the direction of water flow inside the soil in Figure 17. In the soil at further radial distance, gravity mainly induces downward pore water flow. The pore liquid water flow is in the direction of the soil-foundation interface near the interface. The trend of thermally-induced fluid flow will be more obvious as the tests run longer or under higher thermal load [Wang et al., 2014]. Variations of volumetric water content are compared vertically and horizontally between the modeling and experimental results in Figure 19. Similar trends are observed though the experimental results exhibit

slightly higher values. Volumetric water contents are very close at the same radius ($r = 58mm$). While the temperature increases within soil, volumetric water contents rise higher in the region closer to the foundation-soil surface ($r = 58mm$) than in the further region ($r = 101mm$). In the further region ($r = 177mm$), much lower increase of the volumetric water content is observed at the end of Phase 4. But the thermally driven moisture movement might change the distribution of volumetric water content as the temperature gradients become lower within the soil. Further research involving higher temperature gradients and longer-term observations are necessary to investigate the thermally-induced fluid (liquid water and water vapor) flow. Figure 20 presents the average temperature variations of the foundation center and the different positions in the soil during Phase 4. The temperature trend at the foundation center depends on how the prescribed temperature is applied at $r = 24.25mm$. In the simulation, the prescribed temperature linearly ramps up from room temperature (20^oC) to 39^oC during the first 1.35 hours, and then is kept constant for the rest of Phase 4. According to the temperature comparison, the simplified assumption of the thermal boundary condition does not capture the transient trend at the foundation center exactly, but after a certain time (3 hours in this case), the difference becomes negligible when the foundation arrives at the steady-state temperature. The temperature within the soil ($r = 106, 155, 216, 293mm$) changes relatively slow, compared to the foundation.

In an attempt to simulate the failure process during Phase 5 in the centrifuge experiment, the model uses a failure load of $3645N$ estimated from the experimental observations [Goode, 2013] as the ultimate load on the top of the foundation. Figure 21 shows that the settlements corresponding to the ultimate capacity in the experiment are much larger than those from the modeling results. Load-settlement curves from the modeling results imply that plasticity is not reached in the soil continuum under the estimate ultimate load, even though the nonlinear thermo-elasto-plastic constitutive model is applied to the soil continuum. Because of the assumption of a perfect bond at the foundation-soil interface, the model failed to capture the side-shear failure that induced the slippage at the interface and meanwhile contributed to the large settlements in the experiment. We believe that with the interface elements implemented along the foundation-soil interface, the model

can provide more accurate simulation of the failure mechanism in the future.

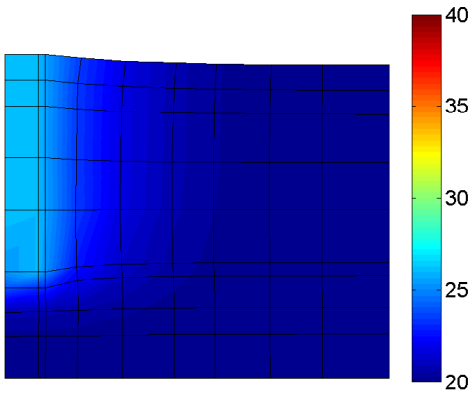

Figure 6. Temperature (^oC) contours at the end of Phase 4 under $\Delta\theta = 6^oC$.

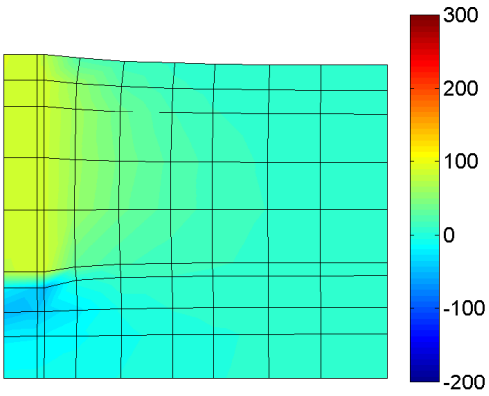

Figure 7. Thermal axial strain $\varepsilon_{zz}(\mu\varepsilon)$ contours at the end of Phase 4 under $\Delta\theta = 6^oC$.

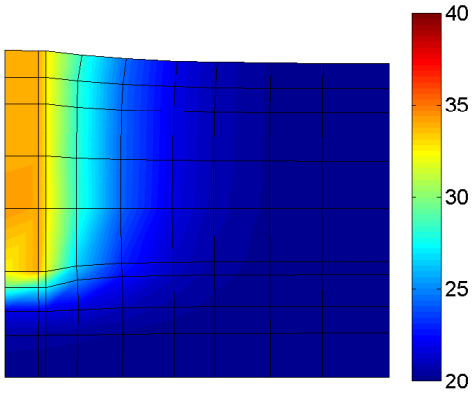

Figure 8. Temperature (^oC) contours at the end of Phase 4 under $\Delta\theta = 14^oC$.

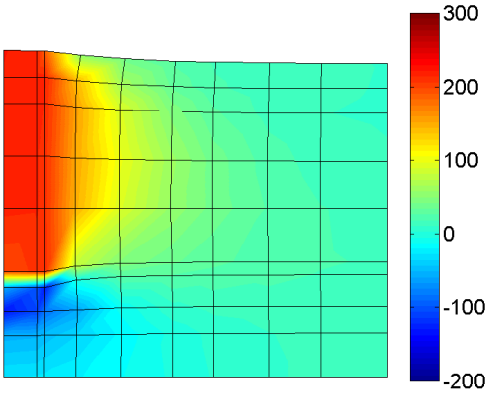

Figure 9. Thermal axial strain $\varepsilon_{zz}(\mu\varepsilon)$ contours at the end of Phase 4 under $\Delta\theta = 14^oC$.

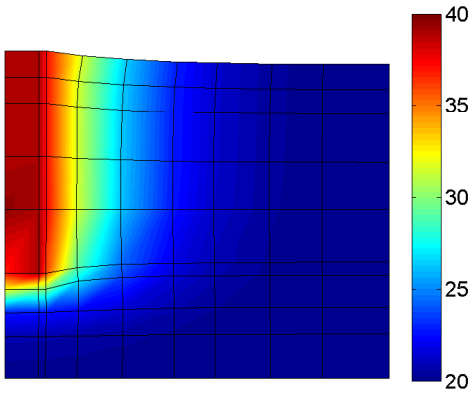

Figure 10. Temperature (^oC) contours at the end of Phase 4 under $\Delta\theta = 19^oC$.

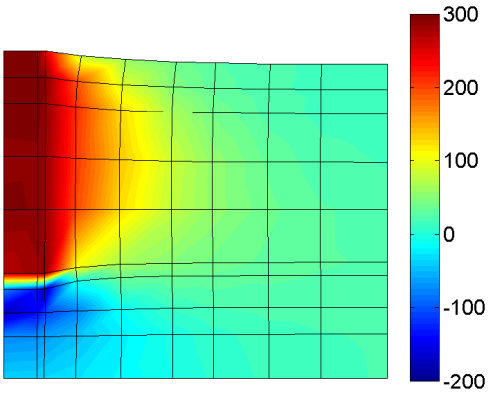

Figure 11. Thermal axial strain $\varepsilon_{zz}(\mu\varepsilon)$ contours at the end of Phase 4 under $\Delta\theta = 19^oC$.

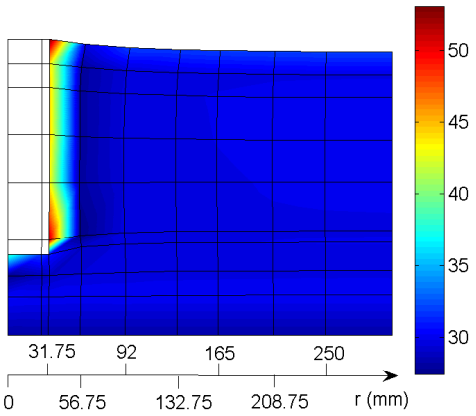

Figure 12. Contours of suction (kPa) in soil at the end of Phase 4 under $\Delta\theta = 19^oC$.

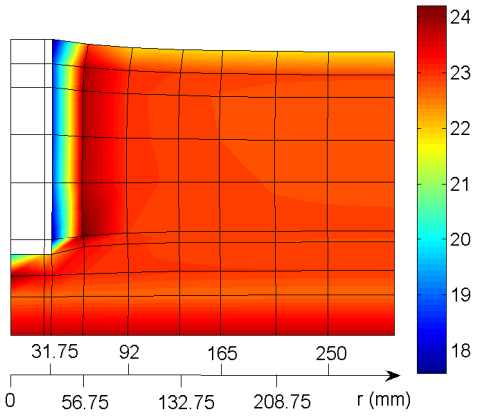

Figure 13. Volumetric water content (%) contours in soil at the end of Phase 4 under $\Delta\theta = 19^oC$.

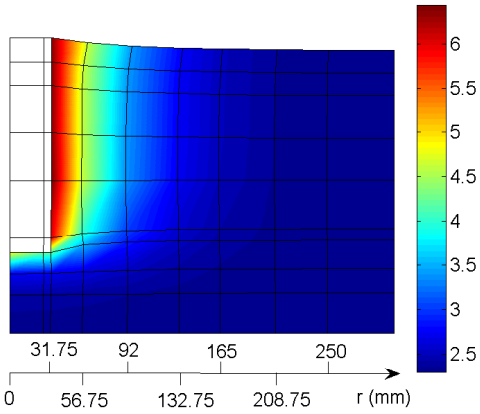

Figure 14. Contours of absolute pore water vapor pressure (kPa) in soil at the end of Phase 4 under $\Delta\theta = 19^oC$.

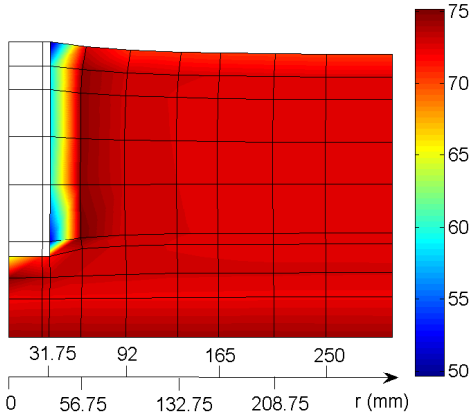

Figure 15. Contours of pore water liquid pressure (kPa) in soil at the end of Phase 4 under $\Delta\theta = 19^oC$.

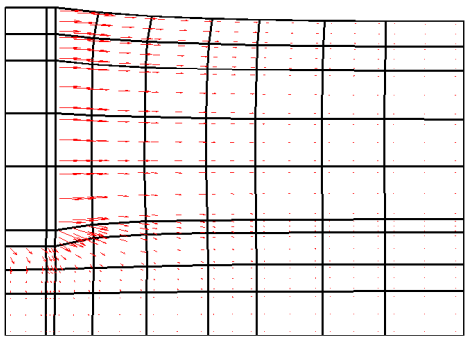

Figure 16. Pore water vapor flow vectors in soil at the end of Phase 4 under $\Delta\theta = 19^oC$.

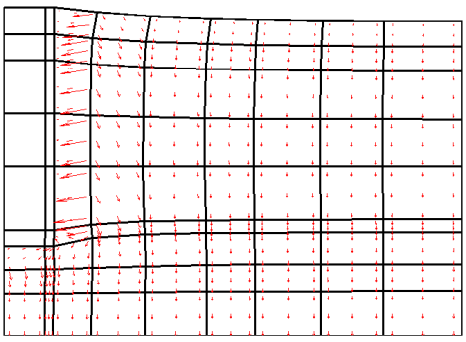

Figure 17. Pore water liquid flow vectors in soil at the end of Phase 4 under $\Delta\theta = 19^oC$.

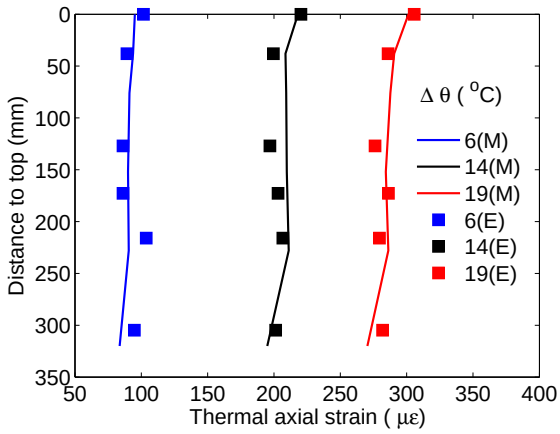

Figure 18. Comparison of thermal axial strain $\varepsilon_{zz}^{\theta}$ within the energy foundations at the end of Phase 4 under different temperature changes between model (M) predictions and experimental (E) data.

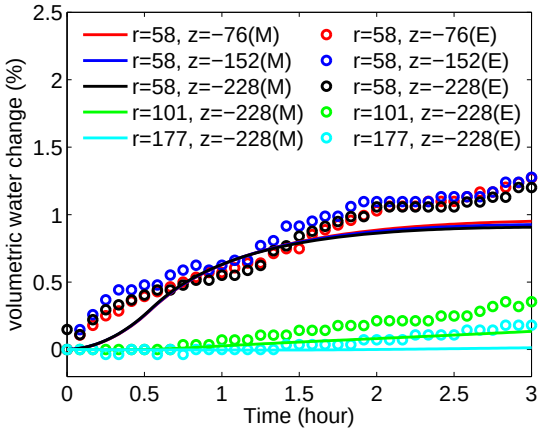

Figure 19. Comparison of volumetric water content within soil during Phase 4 under $\Delta\theta = 19^{o}C$ at different positions (mm) between model (M) predictions and experimental (E) data.

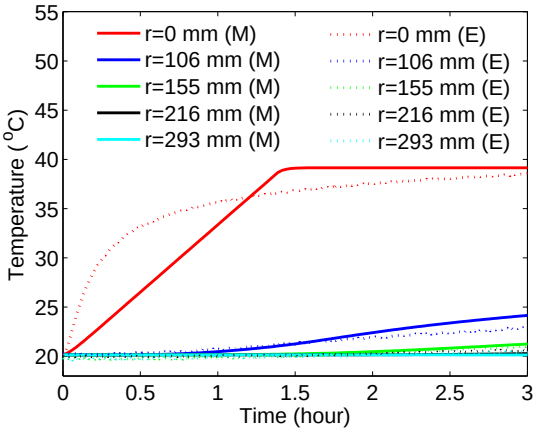

Figure 20. Comparison of temperature variation at the center of the energy foundation ($r = 0mm$) and different radii inside the surrounding soil during Phase 4 under $\Delta\theta = 19^{o}C$ between model (M) predictions and experimental (E) data.

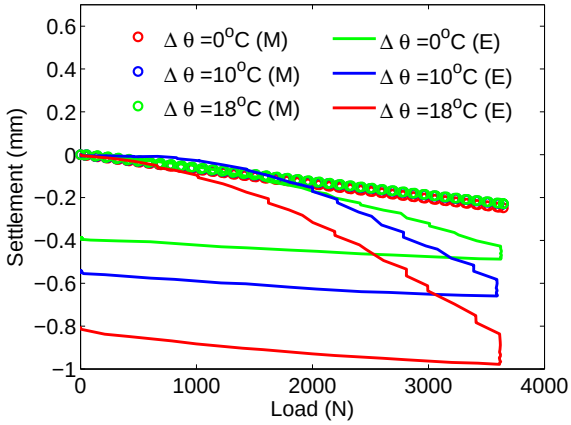

Figure 21. Comparison of load-settlement curves between model (M) predictions and experimental (E) data within soil during Phase 5.

7 Conclusions

The paper applies a small strain, fully coupled thermo-poro-mechanical (TPM) finite element analysis (FEA) of partially saturated, nonlinear elasto-plastic soil solid skeleton to simulate change of temperature, displacement, and strain in an energy foundation as well as suction and volumetric water content in the surrounding soil through SSI. Good agreement with respect to temperature, strain and volumetric water content under the building load is obtained through the comparisons between the modeling and the experimental results. Reasonable explanations are provided regarding the thermally-induced fluid flow. The main issue of the current model is that it can not accurately represent the plastic failure due to the loss of side shear resistance without the implementation of interface elements at the foundation-soil interface. Another issue is the identification of proper thermal boundary conditions. For example, the top ($z = 0$) temperature is simply assumed to be constant (room temperature). This boundary condition could be improved by considering evaporation fluxes at the top of the soil due to soil-atmosphere interaction. In addition, the assumption of prescribed temperature along the direction z at $r = 31.75mm$ in the model does not represent the experimental condition exactly. Extension of the axisymmetric model to 3D and inclusion of a computational fluid dynamics (CFD) analysis for heated fluid flow through the heating tubes within the foundation could resolve this issue.

8 Acknowledgements

Funding for this research was provided by National Science Foundation grant CMMI-0928159. This funding is gratefully acknowledged.

References

O.N. Abdel-Hadi and J.K. Mitchell. Coupled heat and water flows around buried cables. Journal of the Geotechnical Engineering Division, 107(11):1461–1487, 1981.

B.L. Amatya, K. Soga, P.J. Bourne-Webb, T. Amis, and L. Laloui. Thermo-mechanical behaviour of energy piles. Géotechnique, 62(6):503–519, 2012.

J. Bear, J. Bensabat, and A. Nir. Heat and mass transfer in unsaturated porous media at a hot boundary. i. one-dimensional analytical model. Transport in Porous Media, 6(3):281 – 298, 1991.

A.W. Bishop. The principle of effective stress. Teknisk Ukeblad, 106(39):859 – 863, 1959.

A.W. Bishop and G.E. Blight. Some aspects of effective stress in saturated and partly saturated soils. Geotechnique, 13(3):177–197, 1963.

R.I. Borja. Cam-clay plasticity. part v: A mathematical framework for three-phase deformation and strain localization analyses of partially saturated porous media. Computer Methods in Applied Mechanics and Engineering, 193(48):5301–5338, 2004.

P.J. Bourne-Webb, B. Amatya, K. Soga, T. Amis, C. Davidson, and P. Payne. Energy pile test at lambeth college, london: geotechnical and thermodynamic aspects of pile response to heat cycles. Géotechnique, 59(3):237–248, 2009.

H. Brandl. Energy piles and diaphragm walls for heat transfer from and into the ground. Deep Foundations on Bored and Auger Piles, pages 37–60, 1998.

H. Brandl. Energy foundations and other thermo-active ground structures. Geotechnique, 56(2): 81 – 122, 2006.

O. Coussy. Poromechanics. Wiley, 2004.

R. de Boer. Trends in continuum mechanics of porous media, volume 18. Springer, 2005.

D.A. de Vries. Simultaneous transfer of heat and moisture in porous media. American Geophysical Union – Transactions, 39(5):909 – 915, 1958.

D.A. de Vries and A.J. Kruger. On the value of the diffusion coefficient of water vapour in air. In Proc. Of Colloque Int. Du CNRS, number 160, pages 61–72, 1966.

A. Ennigkeit and R. Katzenbach. The double use of piles as foundation and heat exchanging elements. In PROCEEDINGS OF THE INTERNATIONAL CONFERENCE ON SOIL MECHANICS AND GEOTECHNICAL ENGINEERING, volume 2, pages 893–896. AA BALKEMA PUBLISHERS, 2002.

B. François and L. Laloui. Acmeg-ts: A constitutive model for unsaturated soils under non-isothermal conditions. International journal for numerical and analytical methods in geomechanics, 32(16):1955–1988, 2008.

D. Gawin, P. Baggio, and B. A. Schrefler. Coupled heat, water and gas flow in deformable porous media. International Journal for numerical methods in fluids, 20(8-9):969–987, 1995.

J.C. Goode. Centrifuge modeling of the thermo-mechanical response of energy foundations. Master's thesis, University of Colorado, Boulder, U.S., 2013.

J.C. Goode and J.S. McCartney. Centrifuge modeling of energy foundations in sand and clay. In 8th International Conference on Physical Modelling in Geotechnics, in press, 2014.

A. Hepbasli. Current status of geothermal energy applications in Turkey. Energy Sources, 25(7): 667 – 77, 2003.

P.J. Hughes. Geothermal (ground-source) heat pumps: Market status, barriers to adoption, and actions to overcome barriers. Computers and Geotechnics, 2008.

T. J. R. Hughes. The Finite Element Method. Prentice-Hall: New Jersey, 1987.

N. Khalili and B. Loret. An elasto-plastic model for non-isothermal analysis of flow and deformation in unsaturated porous media: formulation. International Journal of Solids and Structures, 38(46-47):8305 – 30, 2001.

L. Laloui and C. Cekerevac. Thermo-plasticity of clays: An isotropic yield mechanism. Computers and Geotechnics, 30(8):649 – 660, 2003.

L. Laloui, M. Nuth, and L. Vulliet. Experimental and numerical investigations of the behaviour of a heat exchanger pile. International Journal for Numerical and Analytical Methods in Geomechanics, 30(8):763 – 781, 2006.

R.W. Lewis and B.A. Schrefler. The Finite Element Method in the Static and Dynamic Deformation and Consolidation of Porous Media. John Wiley and Sons,Ltd, 2 edition, 1998.

J. Lund, B. Sanner, L. Rybach, R. Curtis, and G. Hellström. Geothermal (ground-source) heat pumps–a world overview. GHC Bulletin, 25(3):1–10, 2004.

J.S. McCartney and K.D. Murphy. Strain distributions in full-scale energy foundations. DFI Journal, 6(2):28–36, 2012.

J.S. McCartney and J.E. Rosenberg. Impact of heat exchange on side shear in thermo-active foundations. ASCE, 2011.

P.C.D. Milly. Moisture and heat transport in hysteretic, inhomogeneous porous media: a matrix head-based formulation and a numerical model. Water Resources Research, 18(3):489 – 98, 1982.

K. M. Neaupane and T. Yamabe. A fully coupled thermo-hydro-mechanical nonlinear model for a frozen medium. Computers and Geotechnics, 28(8):613–637, 2001.

J.R. Philip and D.A. de Vries. Moisture movement in porous materials under temperature gradients. American Geophysical Union – Transactions, 38(2):222 – 232, 1957.

M. Preene and W. Powrie. Ground energy systems: from analysis to geotechnical design. Géotechnique, 59(3):261–271, 2009.

S.W. Rees, M.H. Adjali, Z. Zhou, M. Davies, and H.R. Thomas. Ground heat transfer effects on the thermal performance of earth-contact structures. Renew. Sustain. Energy Rev. (UK), 4(3): 213 – 65, 2000.

E. Romero, A. Gens, and A. Lloret. Temperature effects on the hydraulic behaviour of an unsaturated clay. Geotechnical and Geological Engineering, 19(3-4):311 – 332, 2001.

M.A. Stewart and J.S. McCartney. Centrifuge modeling of soil-structure interaction in energy foundations. ASCE Journal of Geotechnical and Geoenvironmental Engineering, in press, 2013.

H.R. Thomas and Y. He. Analysis of coupled heat, moisture and air transfer in a deformable unsaturated soil. Geotechnique, 45(4):677 – 689, 1995.

H.R. Thomas and Y. He. A coupled heat-moisture transfer theory for deformable unsaturated soil and its algorithmic implementation. International Journal for Numerical Methods in Engineering, 40(18):3421 – 3441, 1997.

H.R. Thomas and H. Missoum. Three-dimensional coupled heat, moisture, and air transfer in a deformable unsaturated soil. International Journal for Numerical Methods in Engineering, 44 (7):919 – 43, 1999.

H.R. Thomas and M.R. Sansom. Fully coupled analysis of heat, moisture, and air transfer in unsaturated soil. Journal of engineering mechanics, 121(3):392–405, 1995.

A. Uchaipichat and N. Khalili. Experimental investigation of thermo-hydro-mechanical behaviour of an unsaturated silt. Geotechnique, 59(4):339–353, 2009.

M.T. van Genuchten. A closed-form equation for predicting the hydraulic conductivity of unsaturated soils. Soil Science Society of America Journal, 44(5):892 – 898, 1980.

W. Wang. Coupled axisymmetric thermo-poro-mechanical finite element analysis of soil-structure interaction in partial saturated silt, in preparation. PhD thesis, University of Colorado, Boulder, 2014.

W. Wang, R.A. Regueiro, and J.S. McCartney. Coupled thermo-poro-mechanical finite element analysis of an energy foundation centrifuge experiment in partially saturated silt. In 8th International Conference on Physical Modelling in Geotechnics, in press, 2014.

W. Wu, X. Li, R. Charlier, and F. Collin. A thermo-hydro-mechanical constitutive model and its numerical modelling for unsaturated soils. Computers and Geotechnics, 31(2):155 – 167, 2004.